Transition Analysis for the HIFiRE-1 Flight Experiment

Fei Li,[*] Meelan Choudhari,[**] Chau-Lyan Chang[+]
NASA Langley Research Center, Hampton, VA 23681

Roger Kimmel[#] and David Adamczak[&]
Air Force Research Laboratory, WPAFB, OH 45433

Mark Smith[##]
NASA Dryden Research Center, Edwards, CA 93523

Abstract

The HIFiRE-1 flight experiment provided a valuable database pertaining to boundary layer transition over a 7-degree half-angle, circular cone model from supersonic to hypersonic Mach numbers, and a range of Reynolds numbers and angles of incidence. This paper reports the initial findings from the ongoing computational analysis pertaining to the measured in-flight transition behavior. Transition during the ascent phase at nearly zero degree angle of attack is dominated by second mode instabilities except in the vicinity of the cone meridian where a roughness element was placed midway along the length of the cone. The first mode instabilities were found to be weak at all trajectory points analyzed from the ascent phase. For times less than approximately 18.5 seconds into the flight, the peak amplification ratio for second mode disturbances is sufficiently small because of the lower Mach numbers at earlier times, so that the transition behavior inferred from the measurements is attributed to an unknown physical mechanism, potentially related to step discontinuities in surface height near the locations of a change in the surface material. Based on the time histories of temperature and/or heat flux at transducer locations within the aft portion of the cone, the onset of transition correlated with a linear PSE N-factor of approximately 14.

Nomenclature

f	=	frequency of instability waves
M_∞	=	freestream Mach number
n	=	azimuthal wavenumber
P_∞	=	freestream pressure
Re	=	freestream unit Reynolds number
Re_k	=	roughness Reynolds number based on boundary-layer edge conditions
Re_{kk}	=	roughness Reynolds number based on conditions at the location of roughness height
s	=	surface distance
t	=	time elapsed since the start of the flight experiment
T_w	=	wall temperature
T_∞	=	freestream temperature
N	=	N-factor of linear instabilities
N_{max}	=	maximum N-factor over the length of the cone
X	=	axial coordinate
X_{tr}	=	axial coordinate of transition location
ΔX_{tr}	=	change in transition location
ΔN	=	change in N-factor

[*] Aerospace Technologist, Computational AeroSciences Branch, M.S. 128, AIAA.
[**] Aerospace Technologist, Computational AeroSciences Branch, M.S. 128, Associate Fellow, AIAA.
[+] Aerospace Technologist, Computational AeroSciences Branch, M.S. 128, Senior Member, AIAA.
[#] Senior Research Engineer, Air Vehicle Directorate, 2130 8th St., WPAFB, OH 45433, Associate Fellow, AIAA.
[&] Senior Aerospace Engineer, Air Vehicle Directorate, 2130 8th St., WPAFB, OH 45433.
[##] Aerospace Engineer, Aerodynamics and Propulsion Branch, M.S. 2228.

ε = detune parameters for secondary instability

θ = azimuthal coordinate with respect to windward meridian

I. Introduction

The Hypersonic International Flight Research and Experimentation (HIFiRE) series of flight experiments by the U.S. Air Force Research Laboratories (AFRL) and Australian Defense Science and Technology is designed to demonstrate fundamental technologies critical to the next generation aerospace systems.[1] The first research flight under this series corresponds to the HIFiRE-1 experiment,[1–3] which was conducted in the Woomera Prohibited Test Range in Southern Australia on March 22, 2010. The primary goal of the HIFiRE-1 experiment was to obtain in-flight transitional and turbulent boundary layer heating data on a 7-degree cone-cylinder-flare configuration. The present computational analysis is aimed at characterizing the laminar-turbulent transition over the surface of the HIFiRE-1 cone and comparing the predicted transition behavior with that inferred from the flight measurements. The primary objectives behind this analysis are to test and validate the transition prediction tools, establish transition correlation criteria against flight data, and examine sensitivities of transition characteristics to uncertainties in flight conditions.

References 1 and 2 summarize the design of the HIFiRE-1 flight experiment and the associated pre-flight effort, whereas the analysis of the actual flight data is discussed in Ref. 3. As described therein, the primary configuration for transition measurement in the HIFiRE 1 flight experiment corresponds to a circular cone, 1.1 meters in length, with a cone half angle of 7 degrees and a small nose radius of 2.5 mm. The design angle of attack (AoA) was equal to zero degrees with an estimated in-flight uncertainty of just under 1 degree. Based on preliminary analysis of the flight test data,[3] this design goal was met during the ascent portion of the actual flight experiment. The first and last 45 seconds of the flight were endo-atmospheric (i.e., inside the atmosphere) and, hence, are potentially relevant to post-flight transition studies. A detailed analysis of the various data acquired during the flight experiment is currently in progress at the AFRL and additional supporting analysis is being conducted at NASA. This paper focuses on the accompanying computations involving transition analyses for selected trajectory locations and their comparison with the relevant flight data. For an in-depth discussion of the experimental findings thus far, the reader is referred to Ref. 3. Ref. 4 describes the HIFiRE-1 mission and system performance. Detailed findings from ground test experiments and related computations preceding the flight experiment are reported in Refs. 5-7. The HIFiRE-1 flight experiment also provided aerothermodynamic data for shock wave – boundary layer interaction near the flared region aft of the cone-cylinder segment of the model. However, computational analysis of that data is not addressed in this paper.

Although HIFiRE-1 met its objective of obtaining hypersonic transition data usable for determining flight N-factors, several system failures occurred. These are described in Ref. 4. In terms of the science yield, the failure of the exoatmospheric pointing maneuver was a more serious malfunction, since it caused the vehicle to enter the atmosphere with an angle of attack as high as 40 degrees. Although angle-of-attack oscillations damped and decreased as the vehicle encountered higher density air at lower altitudes, the payload was still at over 10-degree AoA as aerothermal data began to be collected during descent. Fortunately the payload flew unshrouded, i.e. no nose-cone shell covered the experiment. This permitted low-angle-of-attack (AoA < 1 degree) data to be obtained during ascent. Although ascent data was not the primary HIFiRE-1 mission, at least a portion of the ascent data appears to be useful for stability analysis, and is the focus of this paper. The interpretation of boundary layer transition data acquired during descent is more complicated due to the high vehicle AoA, and detailed analysis of the reentry transition is deferred.

Section II below outlines the analysis codes used for transition prediction. Preliminary analysis of the flight data suggests that the initially turbulent boundary layer over the cone begins to laminarize as the HIFiRE-1 vehicle gains altitude. At about 23 seconds into the flight, the transition front moves off the end of the cone, leaving a laminar boundary layer over the cone surface. Results based on linear stability analysis during this ascent portion of the HIFiRE-1 trajectory are presented in Section III, along with a discussion of the uncertainties in computational predictions. Analysis for a single trajectory point selected from the re-entry phase during which the boundary layer goes from initially laminar to turbulent is described in Section IV. Effects of surface roughness in the form of step excrescences in surface height and 3D isolated roughness elements are briefly considered in Section V. Section VI

highlights the initial findings based on advanced prediction methods related to the nonlinear phase of transition during the ascent segment. A summary of the current results is provided in Section VII.

II. Flow Configuration and Analysis Codes

The cone boundary layer was fully turbulent over all sensors immediately after launch. As the vehicle ascended and the Reynolds number decreased, the transition front moved aft over the cone until all sensors showed laminar flow at approximately 23 seconds. The initial turbulent flow appeared to be due to a trip at joints on the vehicle nose tip. The effects of this trip are analyzed in Section V.

For stability and transition analysis, the flight trajectory of interest during the ascent phase is between approximately 16 and 30 seconds. The free-stream conditions during this time interval are listed below in Table I. The free-stream temperature ranges from a minimum of 199.2 K to a maximum of 232.2 K, which occur, respectively, at 21 and 30 seconds into the flight, during which the flight vehicle ascended from 12.22 km to 30.27 km in altitude. The Mach number increases monotonically with time, but stays approximately constant between 21 and 24 seconds. The unit Reynolds number lies between 2.07×10^6 and 21.44×10^6 per meter, peaking at 17.5 seconds and decreasing monotonically thereafter. The temporal variations in the unit Reynolds number, Mach number and temperature are also shown in Figure 1 (with a slightly larger time range than shown in Table I).

Table I. Freestream conditions at selected times during ascent phase.

Time (s)	P_∞ (Pascal)	T_∞ (K)	M_∞	Unit Re (10^6/m)	Altitude (km)
16.0	20637.5	219.7	3.04	20.53	12.22
17.0	17827.1	215.2	3.55	21.31	13.15
17.5	16416.3	213.4	3.82	21.37	13.66
18.0	15011.2	209.9	4.10	21.44	14.22
19.0	12317.9	205.3	4.66	20.58	15.42
20.0	9851.9	201.0	5.07	18.46	16.75
21.0	7753.7	199.2	5.28	15.28	18.15
21.5	6878.1	201.4	5.30	13.42	18.86
22.0	6102.5	203.7	5.31	11.74	19.58
23.0	4811.9	209.2	5.31	8.93	21.03
24.0	3797.0	213.1	5.34	6.91	22.51
25.0	3014.7	219.6	5.36	5.29	24.00
26.0	2389.2	223.2	5.41	4.14	25.52
27.0	1886.1	225.0	5.50	3.29	27.07
28.0	1502.0	228.1	5.58	2.61	28.65
29.0	1185.9	230.2	5.68	2.07	30.27
30.0	934.5	232.2	5.79	1.65	31.92

The mean boundary layer flow over the cone surface was computed on various grids using a second order accurate algorithm as implemented in a finite-volume, structured grid, compressible Navier-Stokes flow solver VULCAN[†]. The VULCAN computations utilized the code's built-in capability to accomplish shock adaptations. An additional NASA code (CFL3D[9]) was also used in select cases for the purpose of validating the VULCAN solutions.

The stability of the computed boundary layer flow was analyzed using the Langley Stability and Transition Analysis Code (LASTRAC).[10] Most of the analysis was performed using parabolized stability equations (PSE), but the classical, quasi-parallel stability theory was also used in select cases. Sutherland's law is assumed to describe the viscosity variation for both the base flow and the unsteady perturbations associated with boundary layer instability waves. Stokes law is assumed for bulk viscosity.

[†] http://vulcan-cfd.larc.nasa.gov

III. N-Factor Correlation for Ascent Phase

A. Mean flow computations and grid convergence

The surface temperature distribution imposed during the mean flow computations was obtained by combining the results of thermal analysis based on axisymmetric, finite element calculations using AFRL's TOPAZ code and the experimental data based on thermocouple measurements. Because no surface temperature measurements are available up to a distance of approximately 0.3 meters from the nose of the cone, the surface temperature distribution within the upstream region was derived from the TOPAZ simulations and was smoothly integrated with the thermocouple measurements at a discrete set of downstream locations.   The TOPAZ computations assumed a boundary layer trip at x ≈ 0.1m from the nose, which gave rise to a moderate overshoot in the estimated temperature distribution in the vicinity of the trip location. For simplicity, this overshoot was removed in the stability analysis. Later sensitivity analysis described below showed that such a temperature variation is immaterial to the boundary layer stability, and its removal is justified. The measured surface temperatures displayed a small rise toward the end of the cone, due to boundary-layer transition. For the purpose of computing the stability characteristics of the underlying laminar basic state, the temperature rise within the experimental data was ignored during mean flow computations, and the temperature distribution within this aft region was simply extrapolated from the upstream locations. Figure 2 shows a representative surface temperature distribution that was used for the mean flow computations at t = 21.5 seconds. For comparison, the surface temperatures estimated using TOPAZ and those based on thermocouple measurements are also shown. The boundary-layer edge Mach number distribution along the cone in all cases remains approximately constant for $x > 0.2$ meters. The boundary-layer edge Mach number at x = 0.55m (mid-cone) is shown in Fig. 3 (a) as a function of time and the ratio of wall temperature to wall adiabatic temperature along the cone are shown in Fig. 3 (b) for selected cases. Similar to many hypersonic flight configurations, the surface temperatures downstream of the nose are considerably smaller than the local temperatures corresponding to an adiabatic thermal boundary condition.   Thus, no significant first mode instability is expected during the selected window from the ascent phase and this was confirmed by the calculations.   The linear instability phase is, therefore, dominated by second mode disturbances. It is noted that, even though the amplification characteristics of both first and second mode instabilities are known to be sensitive to the surface temperature, any residual uncertainty in the estimated temperatures is not expected to have a major impact on the linear stability correlation. The robustness of findings with respect to uncertainty in surface temperatures is directly confirmed in Section II.C below.

The mean flow grid used in most axisymmetric computations has 577 points in the streamwise direction and 513 points in the wall normal direction, of which no fewer than 120 points are clustered next to the cone surface to resolve the boundary layer. For grid convergence tests, a uniformly denser grid with double the number of points in each direction is created and is used for the mean flow computation at one data point, namely t = 21.5 seconds. To ensure that the computational results are independent of the particular codes used, the CFL3D[10] code is also used for the computation at t = 21.5 seconds. Comparisons of results obtained using the two codes are shown in Figure 4, which displays the respective profiles of streamwise velocity and temperature at selected streamwise locations along the surface of the cone. The same figure demonstrates an excellent comparison between the VULCAN results based on the standard and the denser grids. The barely discernible differences between VULCAN and CFL3D results are believed to arise from the fact that the latter code lacks the shock-wave adaptation capability of the former. Typical Mach contours in the first 40 mm length of the cone are shown in Figure 5 for t = 21.5 seconds into the flight. In this case the Reynolds number based on the nose radius of 2.5 mm is approximately 33,554, and the Mach number behind the shock wave is estimated to be approximately 4.8 over most of the cone. This Mach number, coupled with the cold wall conditions (see Fig. 2 and Fig. 3), indicates that the first mode instability should be weak and that the transition behavior is dominated by the second mode instability as confirmed via the stability characteristics outlined in the following subsection.

B. Stability Characteristics and Comparison with Measured Transition Locations

Second mode N-factors (i.e., amplitude ratios relative to the first neutral location) for various frequencies are computed for t =17s through t = 27s, mostly at 1 second intervals, using the linear form of parabolized stability equations (PSE). The maximum N-factor is only 3.5 at t = 17 seconds, but rises rapidly to 13.3 one second later. The maximum overall N-factor of 21.2 is attained at t = 20 seconds. For t > 20s, the maximum N-factor value drops gradually. The N-factors are shown in Figure 6, covering the time range between 17 and 27 seconds and disturbance

American Institute of Aeronautics and Astronautics

frequencies that increment in 25 kHz intervals. Their peak values and corresponding frequencies are listed in Table II.

Table II. Temporal variation of maximum N-factor over the length of the cone and the corresponding second mode frequency during the trajectory segment of interest during ascent.

Time (s)	N_{max}	Frequency (kHz)
17.0	3.5	600
17.5	8.6	600
18.0	13.3	600
19.0	19.5	600
20.0	21.2	550
21.0	19.6	500
21.5	18.3	475
22.0	17.6	450
23.0	13.5	400
24.0	11.3	350
25.0	10.2	325
26.0	8.3	275
27.0	7.6	250

The transition location over the cone surface as a function of flight time is determined by examining the heat flux computed from thermocouple measurements. The times corresponding to both the boundary between laminar and transitional flow (i.e., time for transition onset) and the boundary between transitional and fully turbulent flow (i.e., "end of transition") are plotted as functions of the corresponding location of the surface probe in Fig. 7. The determination of transition is somewhat subjective, and depends on the criteria and type of sensor used for detection. In these results for ascent, transition end is defined as the time at which a well-defined departure from turbulent heat transfer occurs, as measured by thermocouples. Transition onset is the time at which heat transfer appears to have fully relaxed to a laminar value. N-factors at the beginning of transition at selected times (which coincide with the times for which linear stability analysis was performed) are listed in Table III along with the corresponding locations for transition onset given by the fitted curve in Fig. 7. Also listed in Table III (the last column) is a measure of transition location sensitivity, i.e. the change in predicted transition location if the transition N-factor used in the prediction were to change by unity.

Table III. Transition locations, N-factors and transition prediction sensitivity at selected times during flight.

t (s)	X_{tr} (m)	N-factor	$\Delta X_{tr}/\Delta N$ (m)
21.0	0.760	13.5	0.060
21.5	0.805	13.5	0.055
22.0	0.860	13.7	0.050

If one were to use a transition onset correlation of N=13.5 even at earlier times, then the peak N-factor values from Table II would suggest that the HIFiRE-1 model would remain laminar until shortly after t = 18 seconds. The measured data, however, indicate that the boundary layer flow along the aft end of the cone to be turbulent even at t = 17 seconds, where the peak N-factor has dropped substantially below 13.5. The discrepancy related to the low N-factors for t < 18 seconds and the measured onset of transition at all times until approximately 23 seconds suggests that transition over the flight article during those times may have been influenced by other factors, such as spoilers in the form of surface roughness. The possible role of surface roughness in transition over the HIFiRE-1 model is addressed in Section V.B below.

American Institute of Aeronautics and Astronautics

C. Uncertainty Analysis

Several factors influence the accuracy of the N-factor computations presented above and their correlation with the measured transition locations. These include uncertainties in the surface temperature distribution, which must be specified as a boundary condition during mean flow computations; uncertainties in the actual angle of attack during the flight; and uncertainties about the free-stream conditions of the flight at each instant of the trajectory. Additional uncertainty arises from the data reduction process involving the time histories of surface temperature and/or heat flux measured by thermocouples and heat flux gauges, respectively. It pertains to the noise in the measurements and its impact on estimates of the times for transition onset and end of transition. Determining the times for the beginning and the end of transition at a given transducer location also involved some subjectivity as noted previously. A comprehensive analysis of the various errors and uncertainties and their impact will be presented in a future paper after the completion of the data analysis. However, illustrative results pertaining to some of these uncertainties are presented in this section. The effect of changes in the surface geometry due to steps near material discontinuities is addressed in Section V.B.

1. Surface Temperature Distribution

Since no external temperature measurements were available upstream of x=0.3 m, the temperature distribution in this region must be estimated using other means, which was done using thermal analysis based on the finite element code TOPAZ. The largest uncertainty in this calculated temperature distribution comes from the uncertainty in the trip location near the vehicle nose joints that occurred early in flight. Four bounding cases were calculated using the TOPAZ code. Representative results at t=23 seconds are shown in Fig. 8. This figure shows more variation in the detailed nose-tip temperature distributions than Fig. 2 due to a more realistic modeling of the vehicle structure and materials. The limiting cases examined were: fully laminar throughout ascent, fully turbulent, and "hot tip" and "cold tip" cases. The hot and cold tip cases attempt to bound the uncertainty in the nose joint trip behavior. In the hot tip case, the flow was assumed to trip at the nose-tip / isolator junction at x=0.1m and transition to laminar at t=14 seconds. In the cold tip case, the flow was assumed to trip at the joiner / frustum joint at x=0.2m, and transition to laminar at 11.5 seconds. Between the two extreme cases, the wall temperatures differ by more than 100K over the aft portion of the cone (x > 0.2 m). The temperature distributions for the cold tip and hot tip cases differ mostly within the front 0.2 m of the cone. The mean flow computations based on these wall temperature distributions are carried out and second mode N-factors based on these mean flows are shown in Fig. 9. For the turbulent, hot tip and cold tip cases, the peak N-factors and frequencies remain virtually the same at approximately 14 and 400 kHz, respectively, suggesting that the second mode instability characteristics are insensitive to the wall temperature variations encountered in these three cases, which are deemed to bracket the actual surface temperature distribution in flight. For the relatively large drop in wall temperature in the laminar case, the peak N-factor and frequency do indicate a small increase to 15.5 and 425 kHz, respectively. It should be noted that, in the flight experiment, the extreme situation characterized by the wall-temperature distribution of the laminar case does not actually occur and the wall temperature condition is, in fact, very close to the cold tip case.

2. Uncertainty in Angle of Attack

The cone angle of attack was determined from measured surface pressures. The angle of attack of the cone during the ascending phase of the flight is estimated to be under 1.0 degrees prior to t=23 seconds, and less than 0.5 deg prior to t=20 seconds. As a partial measure of the effects of uncertainty in the angle of attack, fully 3-dimensional mean flow computations were carried out at 0.5 degree angle of attack for freestream conditions at $t = 21.5$ seconds. The boundary layer profiles along the windward and leeward planes of symmetry were extracted and used as an effectively axisymmetric base flow for computing the N-factors for second mode disturbances. The N-factor results are shown in Fig. 10. The changes in the maximum N-factors due to the 0.5 degree angle of attack are small, dropping slightly from 19.6 to 18.5 and 18 along the windward and leeward lines, respectively. The peak frequency increases from 475 kHz to 525 kHz on the windward side and to 400 kHz on the leeward side. Computations at 0.5 degree angle of attack was also done for $t = 23$ seconds, and similar results are obtained. These variations reflect the effect of the thinning and thickening of the boundary layers on the respective sides of the cone. Had it been possible to measure the surface pressure fluctuations at such high frequencies during flight, this variation in dominant frequency across the two planes would have provided a sensitive, supplementary measure for the model angle of attack.

3. Freestream Parameters

Uncertainties in freestream parameters were calculated from atmospheric and trajectory uncertainties using standard techniques.[11] Atmospheric uncertainties were created during the reconstruction of the day-of-flight atmosphere.

Uncertainties for trajectory-related parameters, such as geometric altitude and inertial velocity, were in the form of estimated standard deviations that were calculated as a byproduct of the trajectory reconstruction technique.[12]

Figure 11 shows a comparison of relative, 1-σ uncertainties for three free-stream parameters, namely, flow Mach number, static temperature, and pressure altitude. As illustrated by the figure, the relative uncertainties in pressure altitude were higher than those in the Mach number and static temperature. Yet, the maximum estimated uncertainties were very small, at least during the ascent phase. In the case of Mach number, the inertial velocity computed during the trajectory reconstruction had very low standard deviations due to low noise in the acceleration measurements and a well-known starting condition (velocity of zero). Given the small uncertainties in free-stream parameters, no additional computations were deemed necessary to quantify the impact of those uncertainties on the computed N-factors.

IV. Transition during Re-entry Phase

As described in Refs. 3 and 4, the angle-of-attack during the re-entry phase of HIFiRE-1 flight departed substantially from the design value of zero degrees. Transition analyses for the re-entry phase of the HIFiRE-1 flight are ongoing, but the results obtained for a single, selected instant of time are presented in this section. Based on preliminary analysis of the flight data,[4] it was estimated that transition first appears on the cone surface at approximately 483.5 seconds into the flight and the last observed transition corresponds to t = 485 seconds. The trajectory point corresponding to t = 485 seconds was chosen. The Mach number and unit Reynolds number for this case correspond to 7.195 and 8.32×10^6/m, respectively, with the angle of attack being equal to 6.14 degrees. The angle of attack was based on smoothing of the raw AoA estimates based on surface pressure measurements. The selected flow configuration resembles the ground test configuration for quiet tunnel experiments at Purdue University in terms of the cone half-angle and the angle of attack,[13] which supports second mode instabilities along the windward and leeward lines and strong crossflow instabilities in between. Even though the model surface temperatures during the ground experiment are comparable to those in the HIFiRE-1 flight experiment, the free-stream static temperature is considerably lower than that in flight. Because of the considerably higher value of the ratio of model surface temperature to adiabatic surface temperature in the ground experiment, that configuration also supports modest amplification of first mode waves,[14] which is not anticipated in the flight case.

Because of drift issues with a number of surface thermocouples during the exo-atmospheric segment of trajectory, the surface temperature distribution used for the mean flow computation was based entirely upon the thermal analysis using TOPAZ. No grid convergence studies have been performed for this case, so the results are preliminary. Second mode amplification along the windward and leeward planes of symmetry was computed using linear PSE in the same manner as the nonzero AoA case in Section III.C.3. The N-factors along the windward line reach 14 just past the midway point of the cone and approach 23 near the end of the cone. The peak amplification ratios along the windward line are considerably smaller, only about 9.5. The decreased second mode instability is attributed to the substantially modified mean flow along the leeward line as a result of the convergence of the secondary flow from either side.[14]

The instrumentation pattern for the HIFiRE-1 model was designed to provide detailed 2D maps of surface temperature and/or heat flux over the majority of the cone surface. However, as a byproduct of the spinning of the (axisymmetric) cone model during flight,[3,4] one should be able to gain useful information regarding the crossflow transition behavior by using data along the cone meridians with a relatively dense streamwise spacing of surface transducers. Details of the crossflow transition and the accompanying computational analysis will be targeted during the follow-on phase of this effort.

V. Roughness Effects

At least two different types of surface roughness may have influenced the in-flight transition behavior over the HIFiRE-1 model. The first is the diamond (or "pizza-box") trip that was intentionally mounted along the 180 deg cone meridian to provide transition data for an isolated, 3D roughness element. The other type of trip occurred at backward-facing steps intentionally incorporated into joints at the vehicle nose. These steps were designed to accommodate differential thermal expansion among components of the nose assembly, so that the joints would be flush at 23 km during descent. The 3D trip was mounted near X = 0.52 m and had a fixed height of 2 mm, whereas the two step excrescences were located at X = 0.113 m and 0.213 m, respectively, and only crude estimates are available concerning the height of each step at any given time during the window of interest in this paper.

American Institute of Aeronautics and Astronautics

Roughness effects on boundary layer transition at hypersonic speeds is currently an active area of research; however, no reliable physics based prediction tools are yet available. However, because empirical correlations based on selected attributes of roughness geometry and local mean flow parameters are often used in practical applications, it is useful to examine the HIFiRE-1 flight data in terms of those correlations. Even though multiple correlation parameters have been used in the literature,[15–17] only the Re_k and Re_{kk} parameters for both types of surface roughness are examined during this initial phase.

A. Boundary Layer Trip

Temporal variation of the Re_k and Re_{kk} parameters based on the height of the diamond trip near X = 0.525 m of the 180 deg meridian is shown in Fig. 12(a). The overall variation of both parameters is closely analogous to each other, partly because the height of the 3D trip is close to or exceeds the boundary layer height over the ascent portion of interest, so that the ratio of these two parameters is nearly equal to the ratio of the dynamic viscosities at the wall and in the free-stream, respectively. The viscosity values are determined by the respective temperatures, which vary only weakly in time.

Both Re_k and Re_{kk} increase moderately with time for t > 16 seconds, until reaching a peak near t = 18.5 seconds after which they decrease relatively rapidly up to at least t = 30 seconds. Measurements based on the surface transducers in the vicinity of the 180 degree meridian indicate that boundary layer transition along this meridian moves off the cone surface near t = 30 seconds. This corresponds to $Re_{kk} \approx 2200$, which is significantly higher than the correlation based on the ballistic range data for blunt cone models.

B. Step Excrescences

Because of material discontinuities, the surface of the HIFiRE-1 flight model also had two small, backward facing steps at X = 0.113 m and 0.213 m, respectively. The maximum height of both steps over the trajectory segment of interest was estimated, based on pre-flight photographs and shop measurements, to be less than 0.2 mm. As the nose-tip heated during ascent, the step heights would be expected to decrease due to differential expansion, but this effect is not captured in the current analysis which assumes a constant step height of 0.2 mm in order to bound the problem. The variation with time in the Re_k and Re_{kk} values based on both step locations are shown in Fig. 12(b).

Figure 13(a) shows the density gradient contours based on mean flow computations including the steps. Again, to estimate the maximum impact of the steps, the height of each step was set equal to the upper bound of the estimated range (i.e., 0.2 mm), but the contour of the step was both smoothed and tapered to simplify the computational process. In particular, the 0.2 mm wide step takes the shape of a hyperbolic-tangent-function-like curve that smoothly joins the straight cone side at both ends. The compression waves/reattachment shocks emanating from the vicinity of the step are clearly visible in the density contours from Fig. 13(a). Figures 13(b) and 13(c) show the pressure contours on the scale of the step size. The locations of both step excrescences are upstream of the neutral point for the most amplified second mode instabilities and, hence, do not cause any significant change in the amplification characteristics of the second mode instabilities at t=21.5 seconds. This is confirmed by the results shown in Fig. 14 for the N-factors of various frequencies computed using the mean flows with and without the steps, respectively.

According to an empirical correlation from Ref. 19, the maximum allowable height of a 2D backward facing step in a subsonic boundary layer corresponds to $Re_k = 900$; a forward facing step tends to be less effective in accelerating transition and the allowable height for that case corresponds to $Re_k = 1800$. The linear stability analysis presented in Figs. 13 and 14 suggests that, even at the maximum estimated step height of 0.2 mm, the steps are unlikely to have a significant impact on transition at t=21.5 seconds. The corresponding values of Re_k from Fig. 12(b) are more than 3 times larger than the correlation from Ref. 19. This indicates that the correlation therein does not apply to the high-speed flight data analyzed herein.

VI. Nonlinear Effects

As in any transition process, nonlinear mechanisms are ultimately responsible for the breakdown of wave-like disturbances and need to be analyzed to advance transition prediction methods based on higher fidelity methodologies. As described in Section II, the linear amplification phase of transition over the HIFiRE-1 model during the ascent window of interest is dominated exclusively by second mode disturbances. The most amplified second mode disturbances are axisymmetric in nature and the amplification ratios (N-factors) decrease rapidly with increasing wave angles with respect to the flow direction. Because transition to turbulence must entail an energy

cascade in all three dimensions, a likely catalyst for transition onset may involve relatively rapid growth of non-axisymmetric secondary instabilities that are supported by finite amplitude second mode waves. These secondary instabilities might originate from oblique second mode disturbances or other 3D disturbances that are linearly stable. A spatial secondary instability analysis for nonlinear second mode waves over a slender cone with concave curvature was performed in Ref. 14. However, the concave curvature on that model is likely to influence the nonlinear interactions leading to transition onset. Thus, a similar analysis for the circular cone geometry of the HIFiRE-1 model was deemed useful.

To enable a follow-on study of laminar flow breakdown due to secondary instabilities, the nonlinear evolution of second mode disturbances was computed using direct numerical simulations (DNS). The DNS code used for this computation has been extensively validated in the context of transition analysis ranging from linear and nonlinear wave propagation[19] to the laminar breakdown phase of transition.[20] The computational grid was based on the prior experience and, even though no grid convergence analysis was performed, is expected to be adequate for tracking the evolution of the second mode. The trajectory point corresponding to t = 21.5 seconds was selected for this simulation and the nonlinear development of the 475 kHz second mode instability, which reaches a peak linear N-factor of 18.3 at this flow condition (Fig. 6(g)), was monitored after artificially forcing this mode using a surface actuator at an upstream location close to where this mode first begins to amplify. The nonlinear development of this second mode instability is shown in Fig. 14, wherein the contours of density gradient normal to the wall are plotted as a numerical Schlieren flow visualization. The rope-like contours characteristic of nonlinear second mode disturbances[21] are clearly seen. Fig. 6(g) shows that the linear second mode wave at 475 kHz frequency remains unstable until the end of the cone (i.e., up to X = 1.1 m). On the other hand, the contours from Fig. 15 indicate that nonlinear effects cause this disturbance to reach its peak amplitude just past X = 0.85 m, after which it decays rather rapidly, qualitatively analogous to the cone with concave curvature from Ref. 14.

The nonlinearly perturbed flow is extracted at x = 0.846 m, based on which local secondary instability computations are carried out. Figures 16(a) and 16(b) show the growth rates at different azimuthal wavenumbers for the fundamental and subharmonic modes of secondary instability. The fundamental mode has higher growth rates in comparison with the subharmonic modes. The unstable spectra span a wide range of azimuthal wavenumbers (n) with peak local growth rate at approximately $n = 60$ for the fundamental mode. Both types of secondary instability are approximately phase locked with the second mode primary instability. For comparable primary wave amplitudes, these growth rates are comparable to those computed for the compression cone case[14]. At this station the 'S1' subharmonic mode is found to be dominant whereas, in the compression cone case, a fundamental mode has the maximum overall amplification. Conclusions of a similar nature for the present geometry will have to await secondary instability computations at all stations. The growth rate curves in Fig. 14 also indicate coalescence between two branches. Even though the coalescence occurred away from the locally maximum growth rates, it would be essential to examine its global implications. The follow on DNS computations will target this. In addition, the combined evolution of the (primary) secondary mode and the secondary instabilities above will be tracked to understand the details of the transition process and determine whether such mechanisms may be partially amenable to measurement during future flight experiments of a similar nature.

VII. Summary and Concluding Remarks

The HIFiRE-1 flight experiment by AFRL has provided a valuable and, in many ways, unique database pertaining to the boundary layer transition over a circular cone model at varying Mach number, Reynolds number, and angle of incidence. The analysis of the measurement data and the accompanying computational analysis are still ongoing and this paper outlined the initial findings from the latter portion of this effort. Transition during the ascent phase is mostly dominated by second mode instabilities except in the vicinity of the 180 degree meridian, where a roughness element was placed near the middle of the cone to enable measurements of roughness induced tripping. The first mode instabilities were found to be weak at all trajectory points analyzed from the ascent phase. Due to the lower Mach number at earlier times during flight, the peak amplification ratio for the second mode instabilities became sufficiently low for times less than approximately 18.5 seconds, so that the transition behavior inferred from the measurements is attributed to an unknown mechanism, potentially related to step discontinuities in surface height near the locations of a change in the surface material. Based on the time histories of temperature and/or heat flux at transducer locations within the aft portion of the cone, the onset of transition correlated with a linear PSE N-factor of approximately 14. Because of the substantially higher angle of attack during the re-entry segment relevant to transition, it may not be possible to ascertain the differences, if any, between the N-factors for second mode transition between ascent (when the boundary layer goes from initially turbulent to laminar) and descent (when the

boundary layer goes from laminar to turbulent at increasing times) under similar flow conditions. Limited transition analysis for a select trajectory location from the descent portion of the flight trajectory was presented. Additional work is under way to expand the comparison to the remaining portions of the measured data during the flight experiment, as well as to pursue higher fidelity simulations to shed more light on the significant yet unexplained features of the data analyzed thus far.

References

[1] Kimmel, R. L., Adamczak, D., Gaitonde, D., Rougeux, A., and Haynes, J. R., "HIFiRE-1 Boundary Layer Transition Experiment Design," AIAA Paper 2007-534, 2007.

[2] Kimmel, R. L., "Aerothermal Design for HIFiRE 1 Flight Vehicle," AIAA Paper 2008-4034, 2008.

[3] Kimmel, R. L. and Adamczak, D., and DSTO AVD Brisbane Team, "HIFiRE-1 Preliminary Aerothermodynamic Measurements,"AIAA Paper to be presented at 41st Fluid Dynamics Conference and Exhibit, Honolulu, HI, June 2010.

[4] Adamczak, D. and Kimmel, R. L., and the DSTO AVD Team Brisbane, "HIFiRE-1 Flight Trajectory Estimation and Preliminary Experimental Results," AIAA Paper 2011-2358, 2011.

[5] Berger, K., Greene, F., Kimmel, R.L., Alba, C., and Johnson, H., "Aerothermodynamic Testing and Boundary Layer Trip Sizing of the HIFiRE Flight 1 Vehicle," *Journal of Spacecraft and Rockets*, Vol. 46, No. 2, pp. 473-480, 2009.

[6] Wadhams, T., Mundy, E., MacLean, M. and Holden, M. "Ground Test Studies of the HIFiRE-1 Transition Experiment Part 1: Experimental Results," *Journal of Spacecraft and Rockets*. Vol. 45, No. 6, pp. 1134-1148, 2008.

[7] Alba, C., Johnson, H. and Candler, G., "Boundary Layer Stability Calculations of the HIFiRE Flight 1 Vehicle in the LaRC 20- Inch Mach 6 Air Tunnel," AIAA-2008-0505, January 2008.

[8] MacLean, M.; Wadhams, T.; Holden, M.; and Johnson, H. "Ground Test Studies of the HIFiRE-1 Transition Experiment Part 2: Computational Analysis," *Journal of Spacecraft and Rockets*, Vol. 45, No. 6, pp. 1149-1164. November-December 2008.

[9] Rumsey, C. L., Biedron, R. T. and Thomas, J. L., "CFL3D: Its History and Some Recent Applications," NASA TM 112861, May 1997, presented at the Godonov's Method for Gas Dynamics Symposium, Ann Arbor, MI.

[10] Chang, C.-L., "LASTRAC.3d: Transition Prediction in 3D Boundary Layers," AIAA Paper 2004-2542, 2004.

[11] Coleman, H. W. and Steele, W. G., *Experimentation and Uncertainty Analysis for Engineers*, John Wiley & Sons, Inc., New York, 1999.

[12] Karlgaard, C. D., Tartabini, P. V., Blanchard, R.C., Kirsch, M. and Toniolo, M.D., "Hyper-X Post-Flight-Trajectory Reconstruction", *Journal of Spacecraft and Rockets*, Vol. 43, No. 1, 2006.

[13] Wheaton, B. M., Juliano, T. J., Berridge, D. C., Chou, A., Gilbert, P. L., Casper, K. M., Sheen, L. E. and Schneider, S. P., "Instability and Transition Measurements in the Mach-6 Quiet Tunnel," AIAA Paper 2009-3559, 2009.

[14] Li, F., Choudhari, M., Chang, C.-L., and White, J., "Analysis of Instabilities in Non-Axisymmetric Hypersonic Boundary Layers over Cones," AIAA Paper 2010-4643, 2010.

[15] Berry, S. A. and Horvath, T. J., "Discrete Roughness Transition for Hypersonic Flight Vehicles," AIAA-2007-0307, 2007.

[16] Schneider, S. P., "Effects of Roughness on Hypersonic Boundary Layer Transition," AIAA-2007-0305, 2007.

[17] Reda, D. C., "Review and Synthesis of Roughness-Dominated Transition Correlations for Reentry Applications," *Journal of Spacecraft and Rockets*, vol. 39, No. 2, pp. 161-167, 2002.

[18] Nenni,. J. P.and Gluyas,. G. L. "Aerodynamic. Design and Analysis on an LFC." *Surface. Astronautics and Aeronautics*, Vol. 4, No. I, July. 1966.

[19] Jiang, L., Chang, C.-L., Choudhari, M., and Liu, C., "Instability-Wave Propagation in Boundary-Layer Flows at Subsonic through Hypersonic Mach Numbers," *Mathematics and Computers in Simulation*, Vol. 65, pp. 469-487, 2004.

[20] Jiang, L., Choudhari, M., Chang, C.-L., and Liu, C., "Direct Numerical Simulations of Transition in a Supersonic Boundary Layer," AIAA Paper 2006-3224, 2006.

[21] Pruett, C.D., and Chang, C.-L. "Direct Numerical Simulation of Hypersonic Boundary-Layer Flow on a Flared Cone," *Theoretical and Computational Fluid Dynamics*, Vol. 11, No. 1, pp. 49-67, 1998.
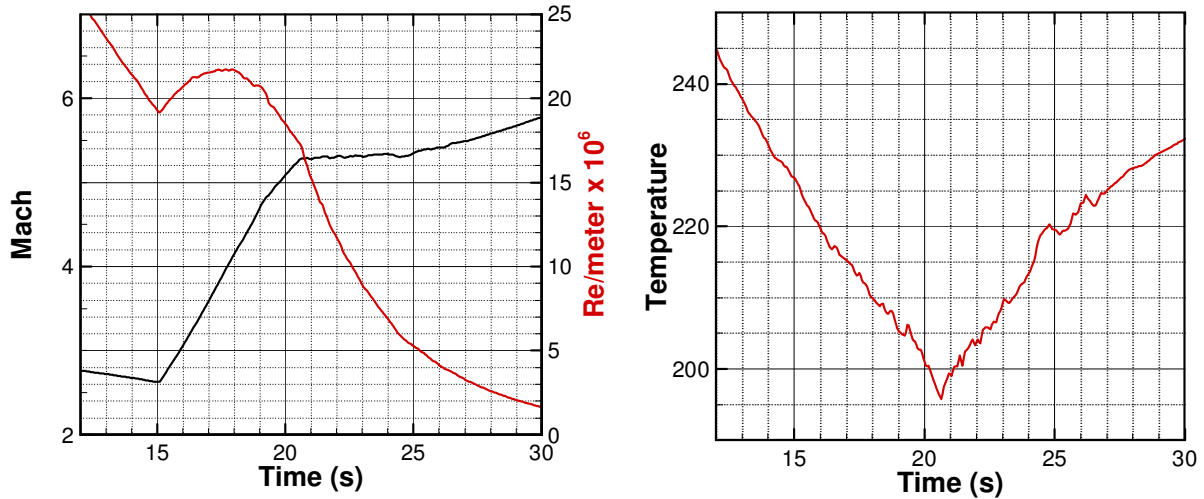
(a) Freestream Mach and unit Reynolds numbers.　　　　(b) Freestream temperature.
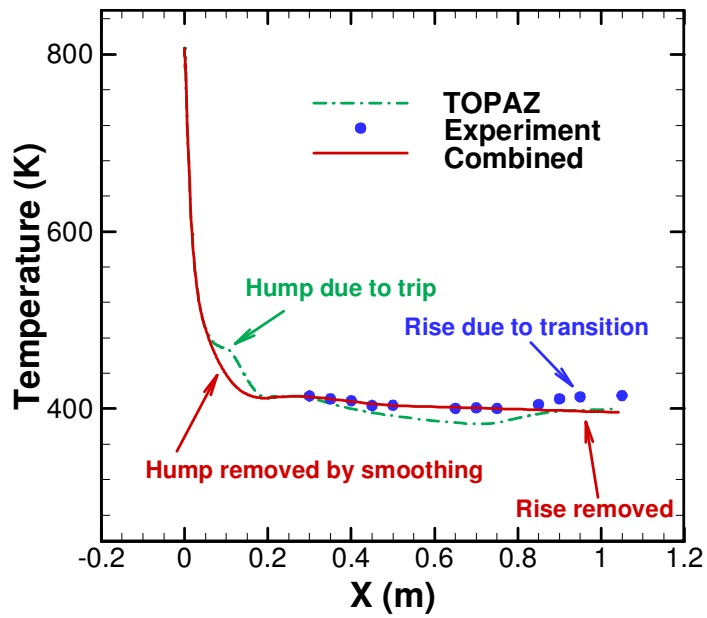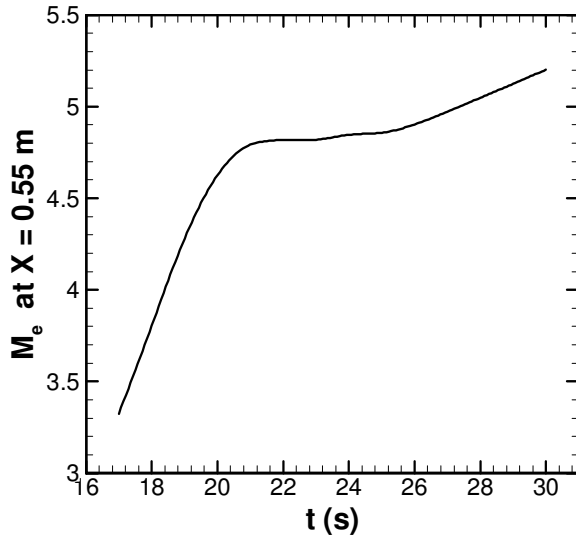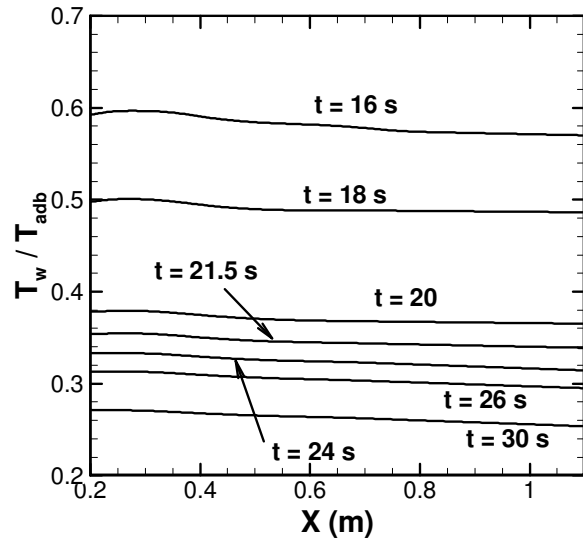
Figure 1. Freestream conditions.
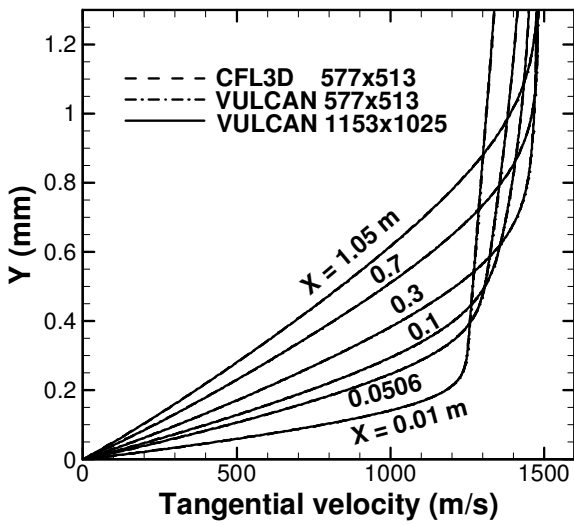

Figure 2. Surface temperature distribution at t = 21.5 seconds.

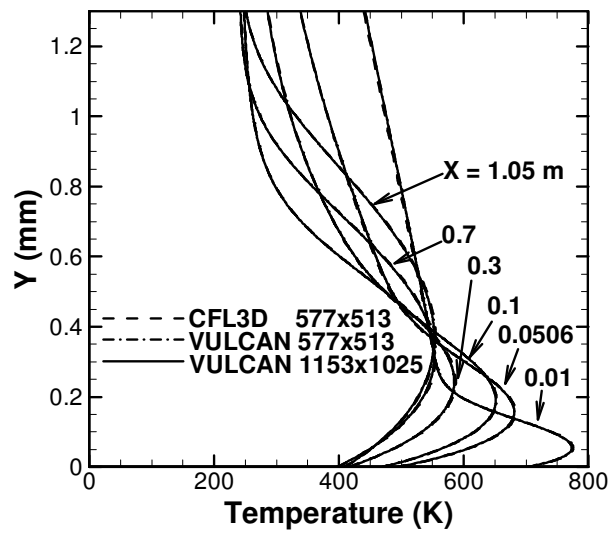American Institute of Aeronautics and Astronautics

(a) Boundary-layer edge Mach number

(b) Temperature ratio

Figure.3 Boundary-layer edge Mach number at x = 0.55m and ratio of wall temperature to wall adiabatic temperature.

(a). Streamwise velocity.

(b) Temperature.

Figure 4. Comparisons of mean flow profiles computed with different grids and codes.
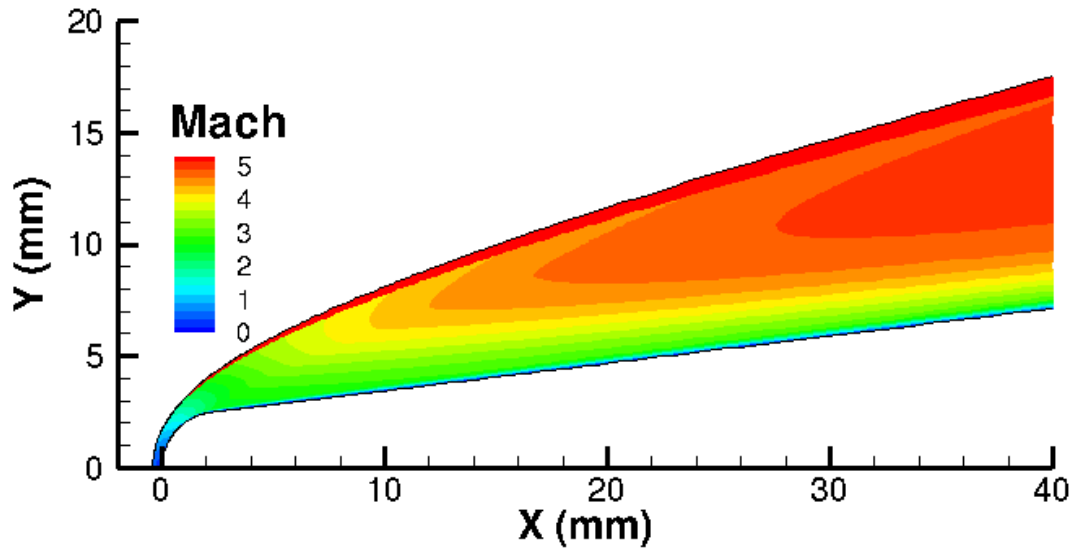
Figure 5. Mach contours near the nose of the cone at t=21.5 seconds.

(a) t = 17 s

(b) t = 17.5 s

(c) t = 18 s

(d) t = 19 s
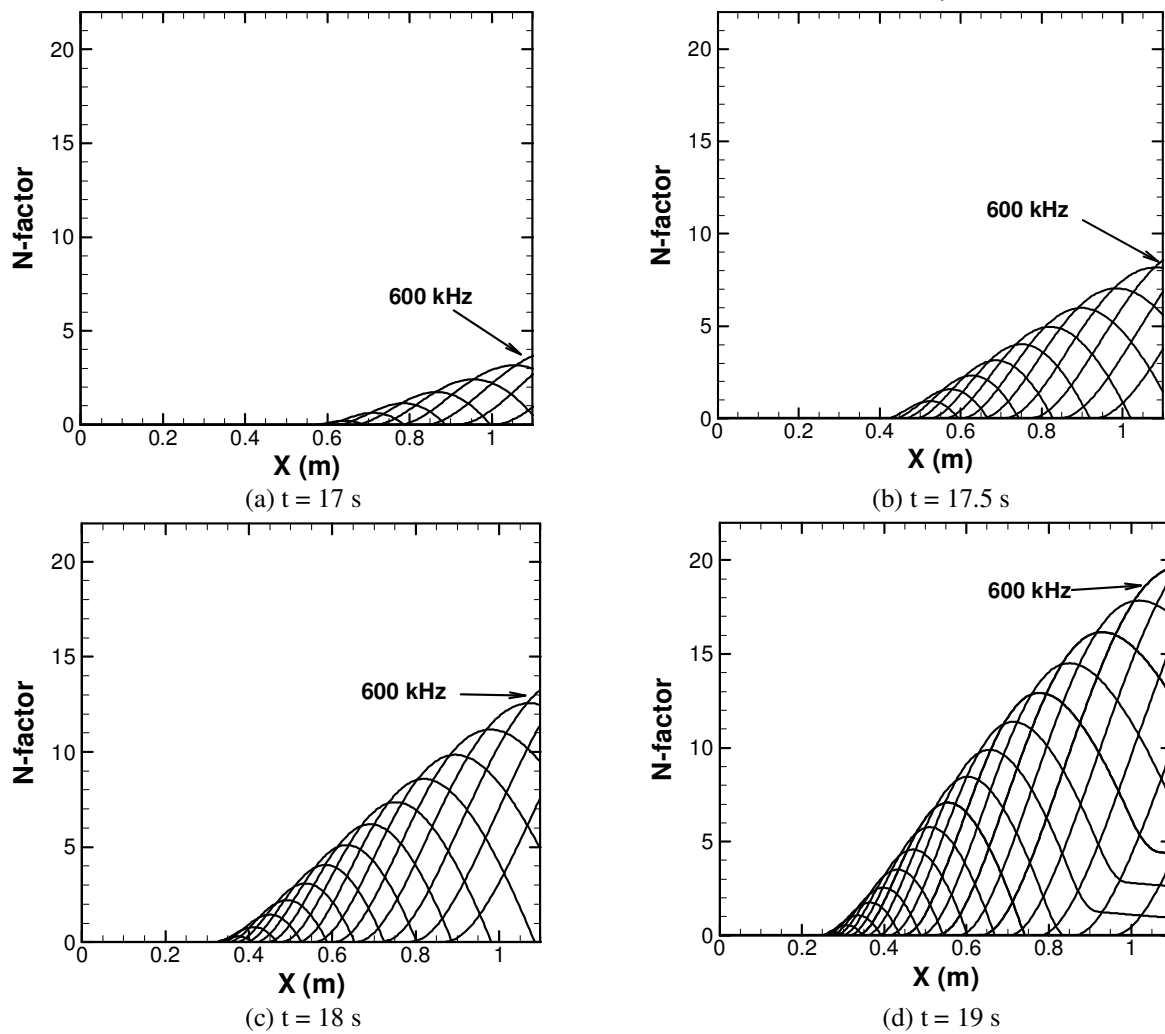
Figure 6 (continued on next page)
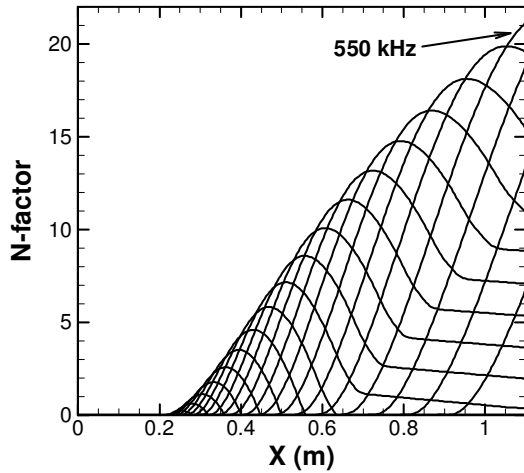
(e) t = 20 s
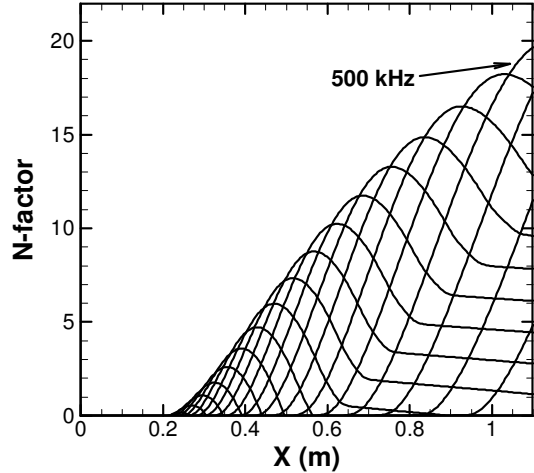
(f) t = 21 s
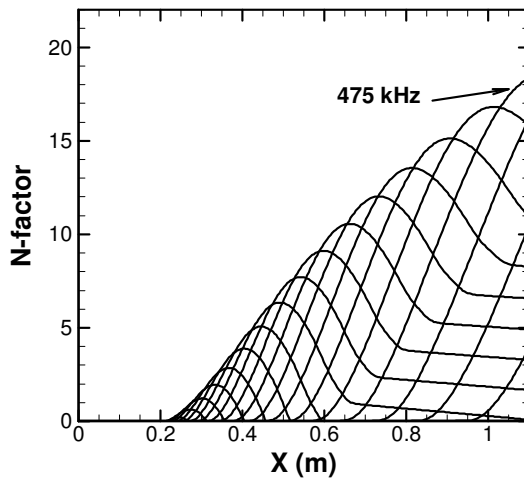
(g) t = 21.5 s
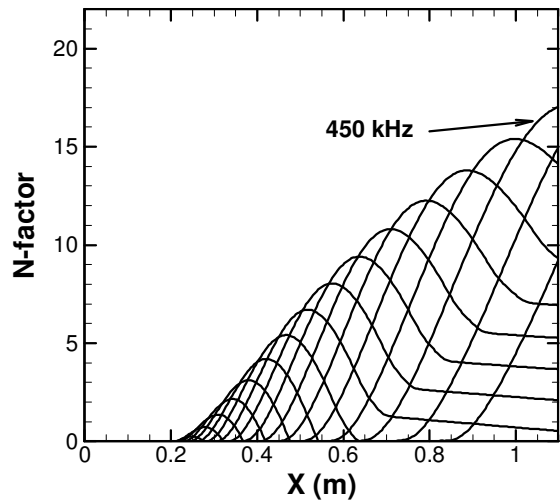
(h) t = 22 s
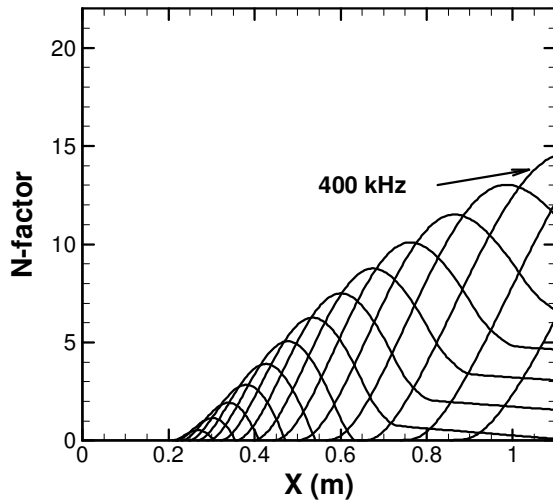
(i) t = 23s
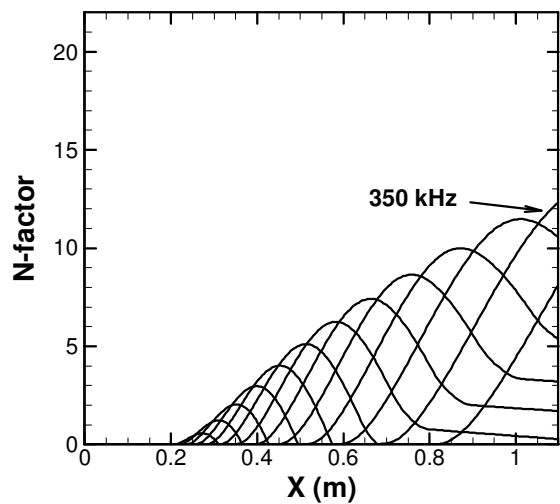
(j) t = 24s

Figure 6 (continued on next page)

(k) t = 25s

(l) t = 26s

(m) t = 27 s
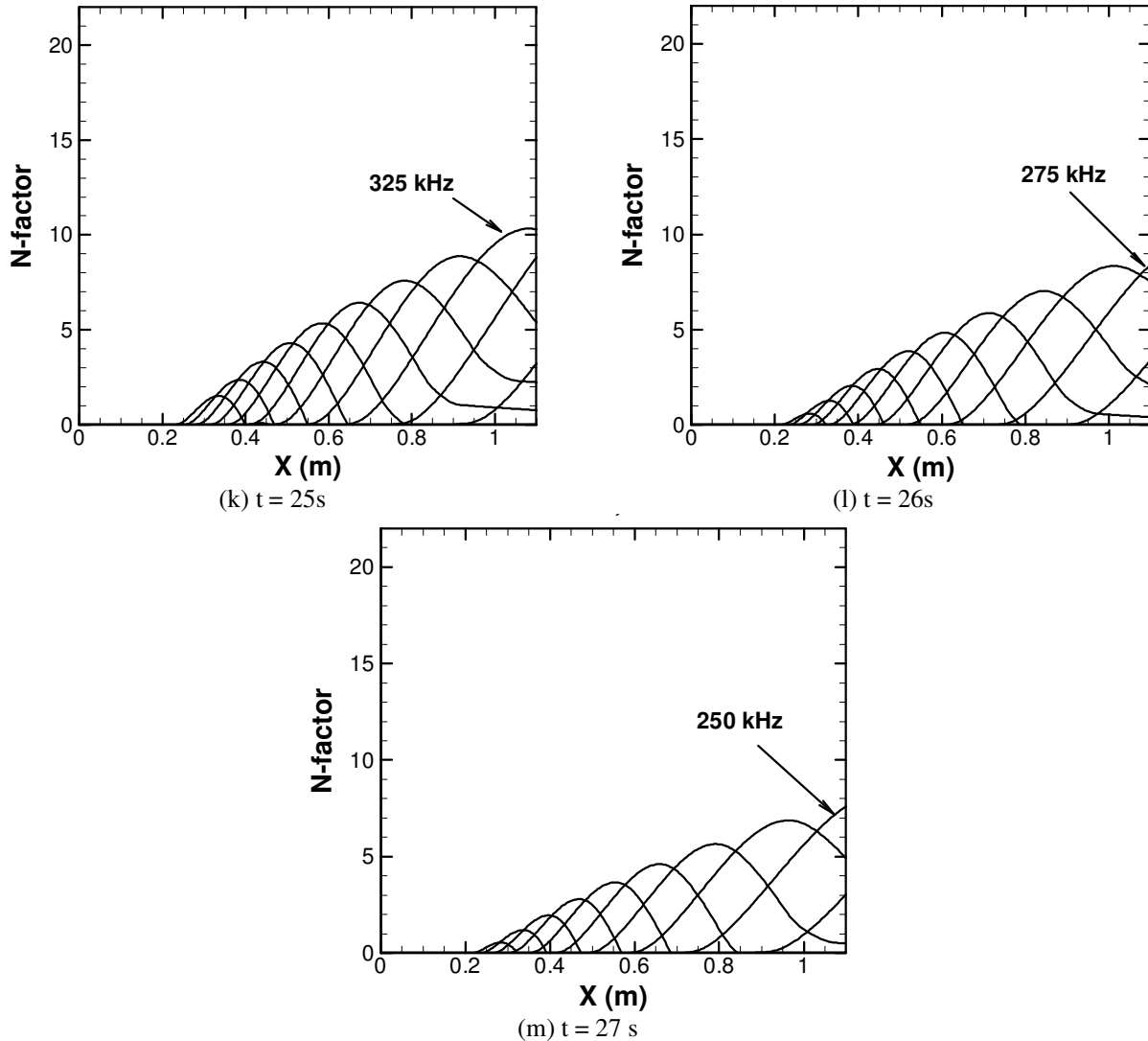
Figure 6. N-factor evolution for second mode disturbances of various frequencies from t = 17 to 27 seconds. The disturbance frequency decreases by 25 kHz across each adjacent pair of N-factor curves.
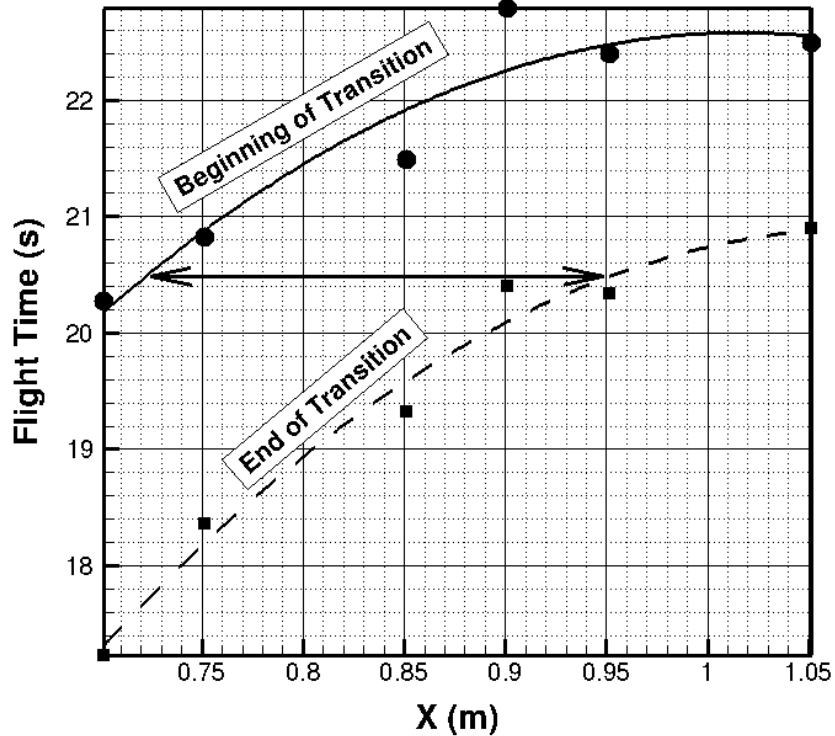
Figure 7. Transition time vs. probe location in the vicinity of the 0 deg meridian along the model. Symbols represent transition locations inferred from experimental data; lines represent 3rd order polynomial fits to the same data. Solid line and round symbols indicate beginning of transition; dashed line and square symbols indicate end of transition. The horizontal black line with arrows at both ends is indicative of the transition region at a fixed instant of time.
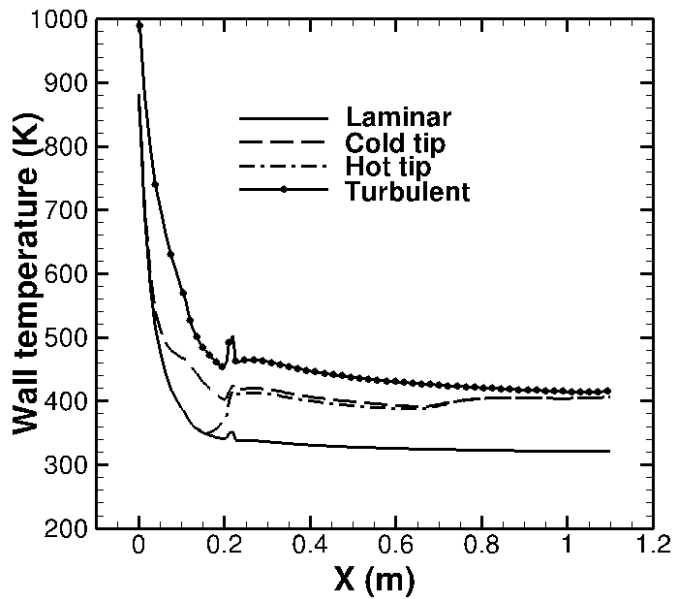
Figure 8. TOPAZ temperature distributions based on different assumptions about wall conditions.
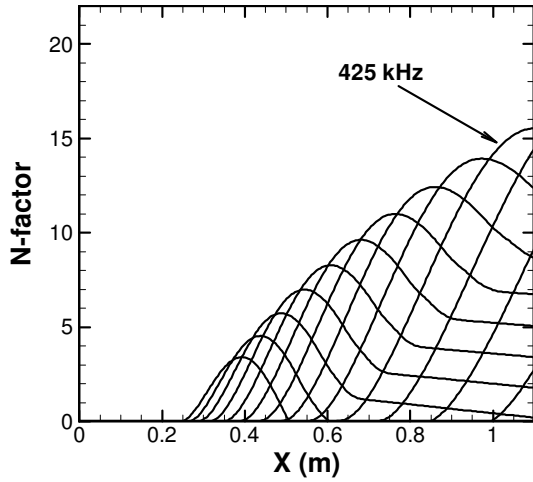
(a) Laminar
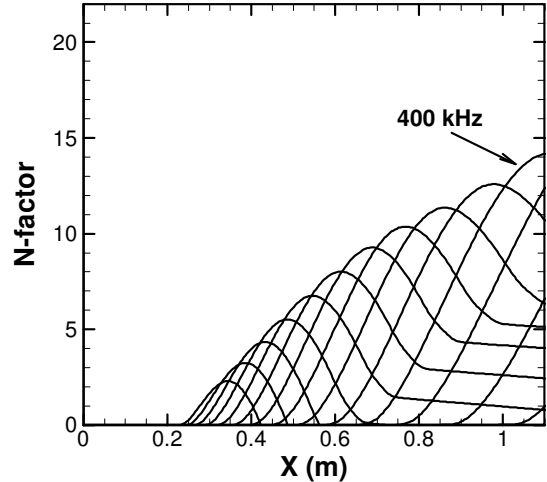
(b) Cold tip
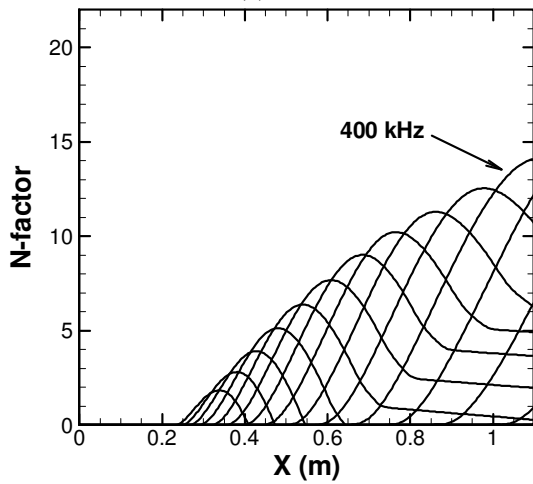
(c) Hot tip
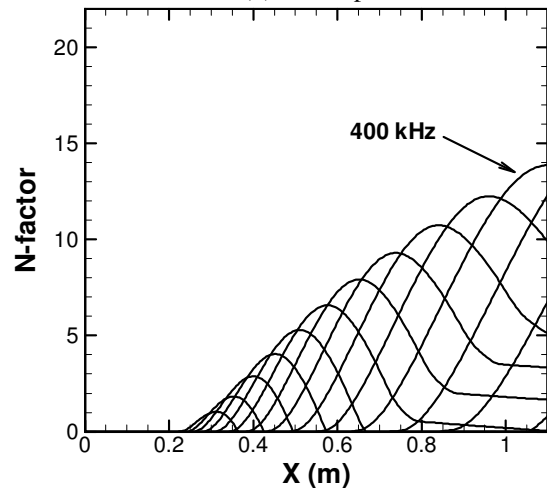
(d) Turbulent

Figure 9. N-factors at t = 23 seconds for different wall temperature distributions.
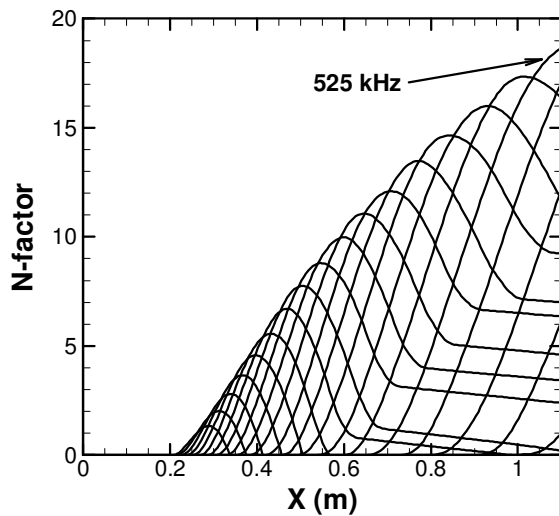
(a) Windward
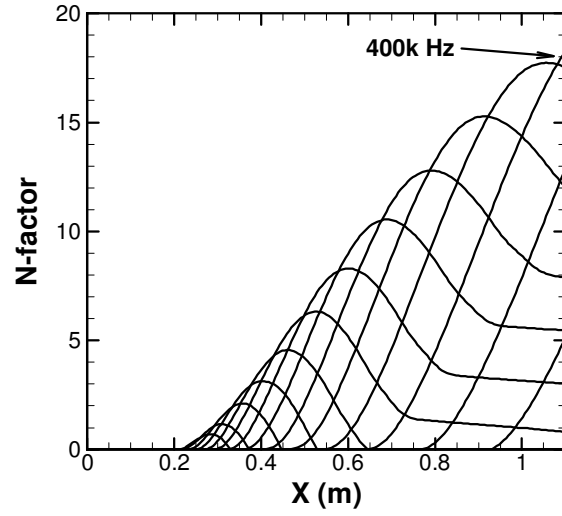
(b) Leeward

Figure 10. Second mode N-factors of various frequencies at 21.5 seconds with a 0.5 degree angle of attack.
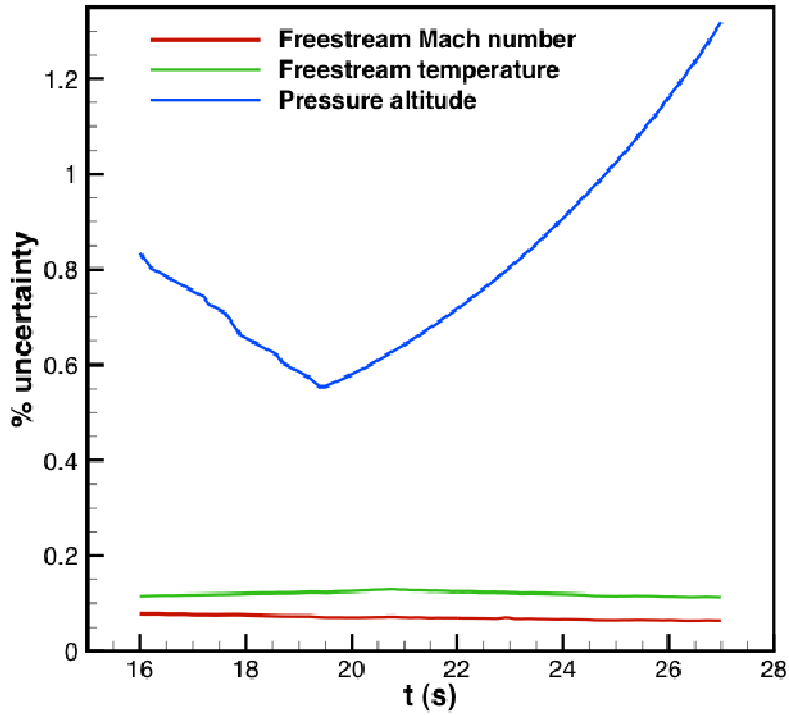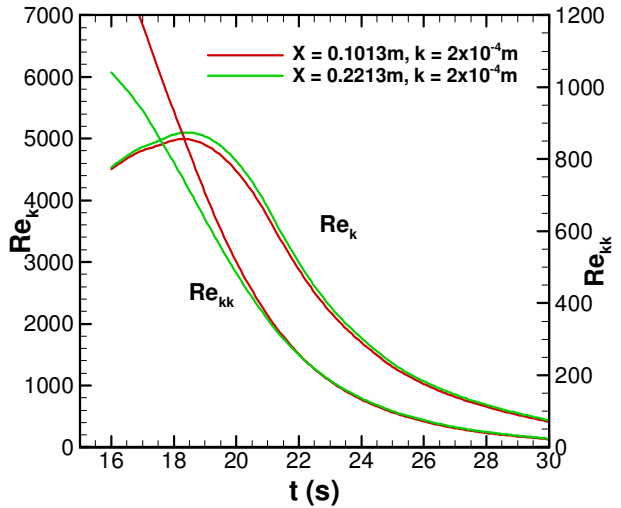
Figure 11. Estimated uncertainties in free-stream parameters.
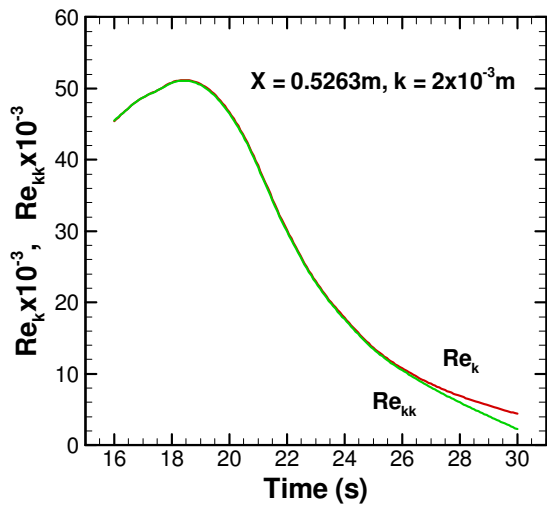

(a) 3D diamond shaped trip

(b) Step excrescences

Figure 12. Temporal variation on Re_k and Re_{kk} parameters corresponding to axisymmetric steps and 3D isolated trip on the HIFiRE-1 model. The plot includes only that portion of the ascent phase which is relevant to boundary layer transition.

American Institute of Aeronautics and Astronautics

(a) Density gradient
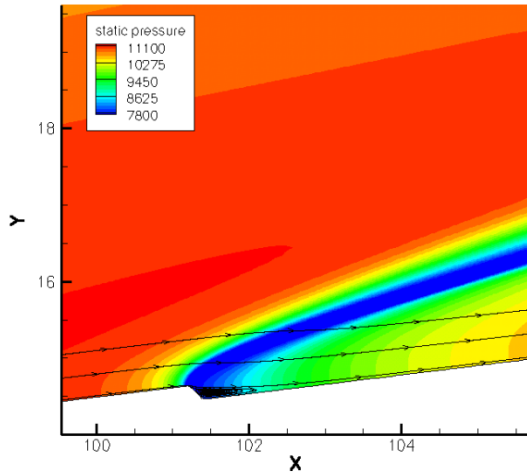
(b) Pressure contours and selected streamlines in neighborhood of first step.
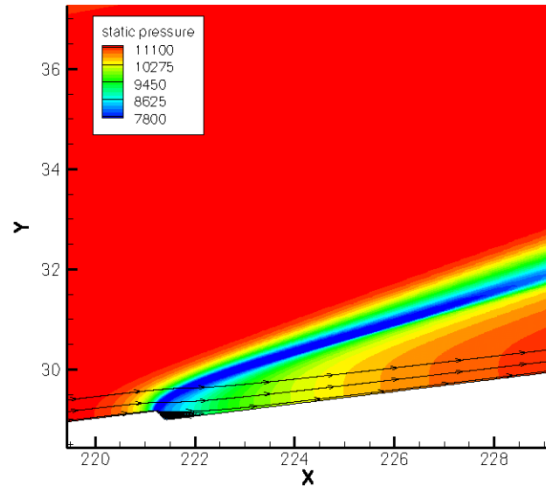
(c) Pressure contours and selected streamlines near second step.

Figure 13. Computed flow field with surface steps at t = 21.5 s.
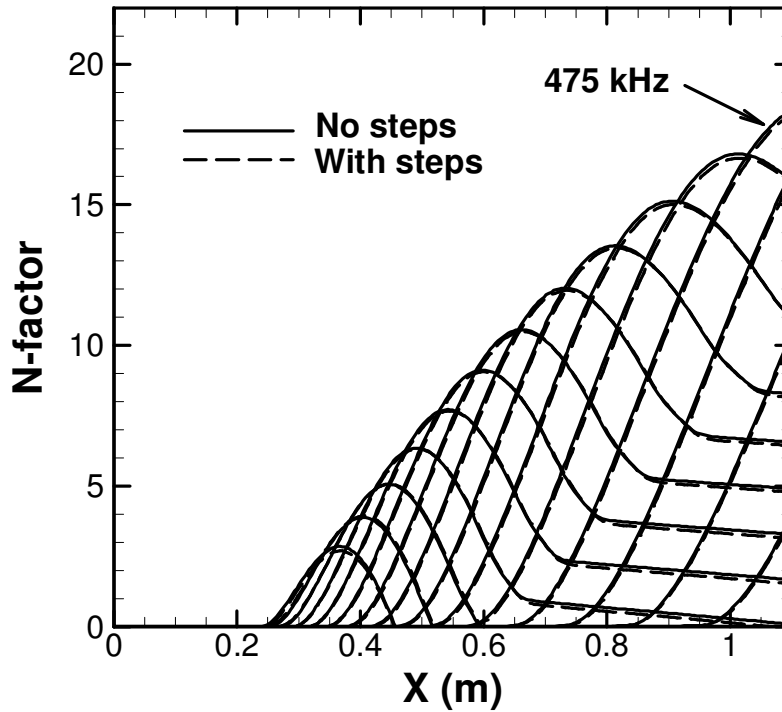

Figure 14. The two steps on the surface of the cone do not alter second mode instability characteristics in any significant way. Red and green lines are N-factors based on mean flow with and without the steps, respectively.
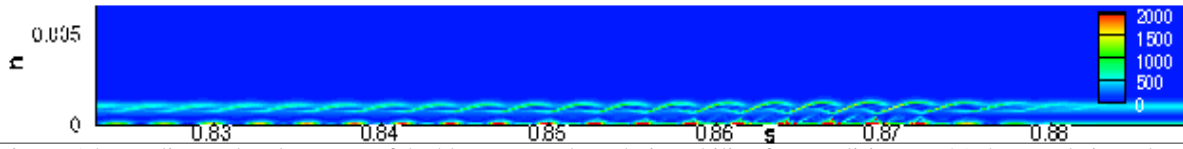
Figure 15. Nonlinear development of 475 kHz second mode instability for conditions at 21.5 seconds into the flight. Flood contours show the normal density gradient in the presence of large amplitude second mode waves. The coordinates s and n correspond to the distance from the nose tip along the cone surface and the wall normal coordinate, respectively. Both coordinates are measured in feet in this figure.
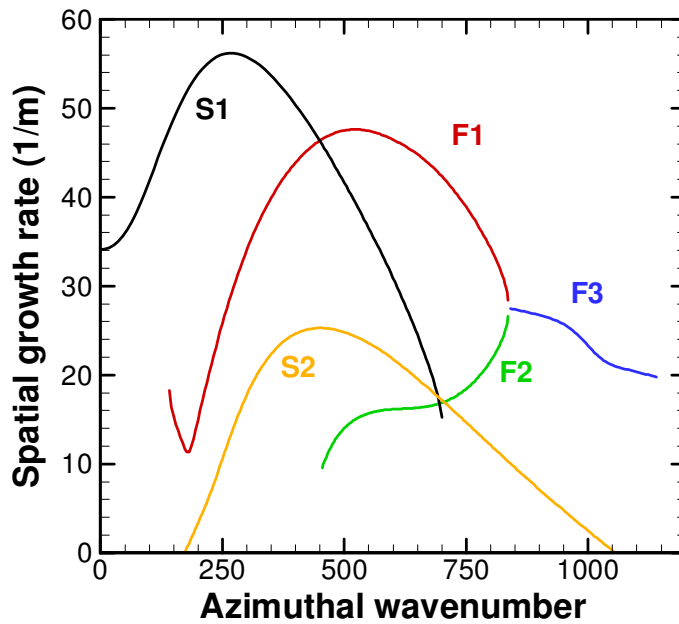

Figure 16. Growth rates of secondary instability modes at a selected location (X = 0.846 m). Lines marked with F and S represent fundamental and subharmonic modes, respectively.

American Institute of Aeronautics and Astronautics